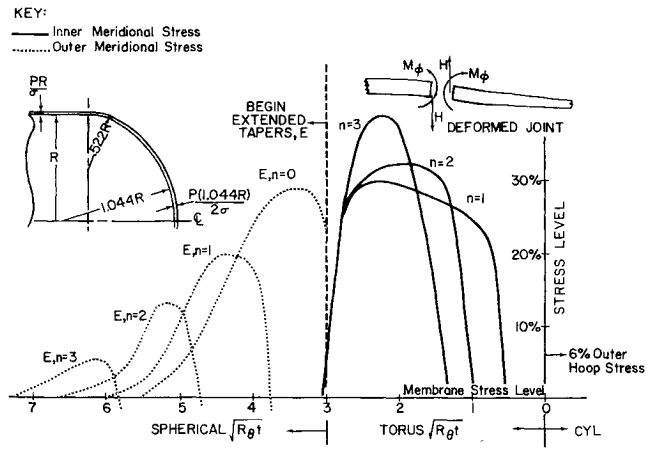

Fig. 2 Stresses in a torispherical head with tapered transition sections.

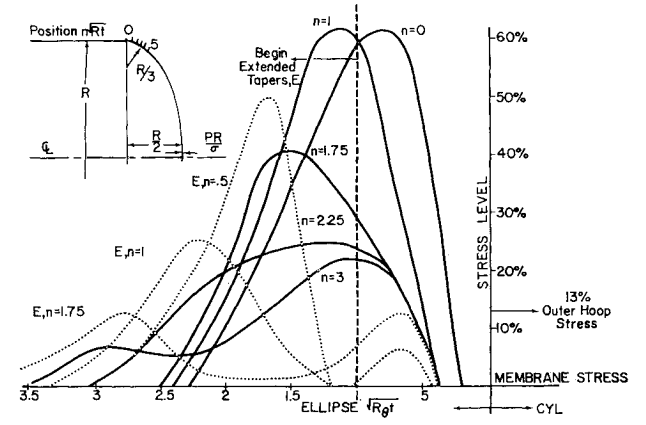

Fig. 3 Stresses in a 2:1 ellispoidal head with tapered transition sections.

section has a 6% stress peak at about 2 characteristic lengths from the torus-cylinder joint). For the latter transitions, stresses below membrane level were calculated in the toroidal section; this indicates that a double taper would reduce the transition section weight (a good subject for further study).

Ellipsoidal Head—Cylinder Juncture (Fig. 3)

The discontinuity stresses at the juncture of a 2:1 ellipse and a cylinder are high, because the ellipse has an equal but compressive membrane stress in the hoop direction. The stresses are particularly high in the meridional direction in the "knuckle" of the ellipse. The head studied here has a constant thickness and a weight equal to that of the hemispherical head; its thickness is 65% of that of the cylinder. (An excellent analysis of ellipsoidal heads has been made in Ref. 4, which substantiates the stress levels noted here.)

Maximum stresses for linear tapers with $n = 0$, 1.75, 2.25, and 3 are shown in Fig. 3. For $n \leq 1$, maximum stress level is 60% above membrane stress level; for $n = 2.25$ to 3, it has fallen to about 22% of the cylindrical membrane stress level. The maximum allowable n is probably near 3, because this would give a tapered length equal to 20% of the head surface length for a shell of $R/t = 100$. Marked reductions in stress are noted when "extended" tapers (E, n curves) are used. (The full thickness of the cylinder is carried 1 characteristic length into the knuckle of the ellipse, then the wall section is thinned to the required 65% of the cylinder thickness.) Maximum stresses now occur on the exterior wall rather than the interior, caused by a change in bending moments. These bending stresses are reduced when the taper covers 1.75 characteristic lengths. (Longer tapers were not used, because bending stresses increased at the juncture, which caused an increase in the hoop stresses in the cylinder.) The maximum stress levels in the cylinder and the ellipse for this "E, $n = 1.75$" taper are approximately equal—about 12% higher than the maximum cylindrical membrane stress.

Conclusions

Design guides have been developed for tapered transition sections for thin-shell ($500 > R/t > 50$), minimum-weight pressure vessels. For the hemispherical head-cylinder joint, a linearly tapered transition $2(R_\theta t)^{1/2}$ in length on the head side will reduce the discontinuity stress level to within 5% of the membrane stress; the maximum stress level will occur at the thin end of the taper; and, therefore, all welds should be removed from that immediate area. For maximum stress reduction, the taper should be faired into the head.

For the torispherical shell of Fig. 2, the taper should be placed on the spherical side of the joint over two characteristic lengths. The resulting meridional stress level in the head will be within 6% of the cylinder membrane stress level. A hoop stress peak of the same magnitude will be apparent in the cylinder at a position 2 characteristic lengths for the joint.

For the 2:1 ellipsoidal head of constant thickness, the taper should begin one characteristic length in from the joint and should cover 1.5 to 2 characteristic lengths of the ellipsoidal surface.

In summation, minimum-weight pressure vessel design requires that bending stresses be reduced wherever possible. This can be done by the use of tapered transition sections at the juncture of dissimilar shells. However, the design of these transition sections is related closely to the geometry of the head except in the case of the full hemisphere. Therefore, in nonhemispherical closures, caution should be exercised when the transition section is designed.

References

[1] Novozhilov, V. V., *The Theory of Thin Shells* (P. Noordhoff, Ltd., Groningen, The Netherlands, 1959), p. 292.

[2] Adkins, A. W., Dingwell, I. W., Pearson, C. E., and Sepetoski, W. K., "A digital computer program for the general axially symmetric thin-shell problem," Trans. ASME (Am. Soc. Mech. Engrs.), Ser. E: J. Appl. Mech. **29**, no. 4, 655–661 (1962).

[3] Hoffman, G. A., "Minimum weight proportions of pressure-vessel heads," Trans. ASME (Am. Soc. Mech. Engrs.), Ser. E: J. Appl. Mech. **29**, no. 4, 662–668 (1962).

[4] Kraus, H., Bilodeau, G. G., and Langer, B. F., "Stresses in thin-walled pressure vessels with ellipsoidal heads," Trans. ASME (Am. Soc. Mech. Engrs.), Ser. B: J Eng. Ind. **83**, no. 1, 29–42 (1961).

Solar Simulation in Space Environment

ALLAN D. LEVANTINE* AND ROBERT P. LIPKIS†
Space Technology Laboratories, Inc., Redondo Beach, Calif.

AT present solar simulation is in its infancy. Evolution of the art has not yet reached the point where the trend toward standardization of design has manifested itself. Many current solar simulator systems represent compromises from the ideal. In the following paragraphs some of the more important design factors being used and the types of errors

Presented as Preprint 63-57 at the IAS 31st Annual Meeting, New York, N. Y., January 21–23, 1963; revision received November 4, 1963.

* Section Head, Solar Simulation Laboratory, Mechanics Division.

† Manager, Spacecraft Heat Transfer Department, Mechanics Division. Member AIAA.

Table 1 Absorptance error for typical spacecraft materials irradiated by mercury-xenon lamps, xenon lamps, and the STL carbon arc system

Material	STL carbon arc[a]		Hg-Xe lamp		Xe lamp	
	error,[b] %	T error[c], °F	error, %	T error, °F	error, %	T error, °F
1) Anodized aluminum 1199 Al foil	−4.6	−6.0	+ 5.3	7.0	− 7.2	− 8.9
2) Titanium oxide film no. 62-60	−3.5	−9.2	+ 6.2	16.0	+ 5.2	+13.7
3) White alkyd resin paint mil-E-10687	−2.0	−2.7	+23	32.1	− 5.3	− 7.1
4) Oxide, evap. titanium on Al foil	−0.3	−0.7	+ 7.7	16.9	+ 0.7	+ 1.6
5) Solar cell with 3 mil glass cover and UV cut-off filter	−3.8	−6.1	− 4.0	− 7.5	+13.7	+22.2

[a] As modified by the optical elements.
[b] % error relative to Johnson-NRL result.
[c] For normally oriented flat plate.

they induce into the simulated space environment are discussed.

A. Sources

The source of radiant energy must have a spectral distribution closely approximating that of the sun. Several available sources are suitable to varying degrees for this purpose; these are the carbon arc, the mercury-xenon lamp, and the xenon lamp. A meaningful way to evaluate the spectral distribution of these sources is in terms of the absorptance α_{ss} of various typical materials which would be subject to irradiation by the simulators as compared to the absorptance α for the Johnson-Naval Research Laboratory solar spectrum. Several typical materials with known spectral absorptance properties have been integrated over the various spectrums. The resulting absorptances are compared in Table 1.

These results are subject to some qualifications because of uncertainties in the material properties and the source spectra, so that the results shown in Table 1 are somewhat qualitative. Nevertheless, the results show that errors can be substantial, and that in general the carbon arc provides a better spectral match than either of the high-pressure arc lamps.

B. Projection Systems

Two fundamental types of projection systems are applicable to solar simulation, the "direct projection system" and the "collimated system." Systems are usually considered direct projection when the source is re-imaged through a chamber port, directly or indirectly, onto the test object. This differs from the collimated system in which the source is projected to a parabolic reflector within the chamber.

An advantage of the direct projection system is that it requires no optical elements within the chamber. However it has two characteristics that make it unsuitable for many thermal tests.

1) It is basically a divergent system. Therefore the incident energy flux crossing any plane perpendicular to the beam will vary approximately inversely as the square of the distance of that plane from the apparent source.

2) The divergent nature of the beam will produce incident angles on the surface of the object or spacecraft different from those occurring in space.

A significant error for a large divergence angle can result from incorrect incidence angles of energy impinging on a surface. Results are shown in Fig. 1 (an insulated flat plate with specified coating properties on its front face) for a simple example. The error in temperature for several incidence angles is shown as a function of the solar simulator divergence angle. (This figure does not include the effect of change in intensity with distance from the source.) Note that this effect alone can produce extremely large errors, especially for shallow (near grazing) incidence angles, which are likely to occur on radiator surfaces.

The collimated system does not suffer from these drawbacks. Intensity does not change with distance, as the rays are all relatively parallel throughout the test volume. Moreover, the direction of the apparent sun is unchanged for points off the central axis.

C. Optical Elements within the Simulation Chamber

Collimated systems normally have parabolic reflectors within the chamber which change the diverging rays to a collimated beam. Two types of collimators are used. These are the cassegrainian, on-axis collimator, which projects light from a source at its center, and the off-axis collimator, which projects light at an angle from a remote port on the chamber wall. Two principal kinds of thermal errors can occur from these elements: 1) reflection errors and 2) emission errors.

Reflection errors arise when the spacecraft can see any part of itself in the simulator optics. If radiation, either reflected solar or infrared emitted, leaving the spacecraft is reflected back to the spacecraft from the collimator optics, substantial errors in incident flux can exist. This type of error is common to the on-axis (cassegrainian) system, where it is impossible to prevent some radiation from returning to the spacecraft. The error can be minimized if the solar simulator beam is small in area and the chamber is sufficiently long to allow a small shape factor from the spacecraft to the collimators.

These reflection errors can be eliminated completely for the off-axis system, by properly positioning the collimators at appropriate angles, so that all reflected or emitted energy

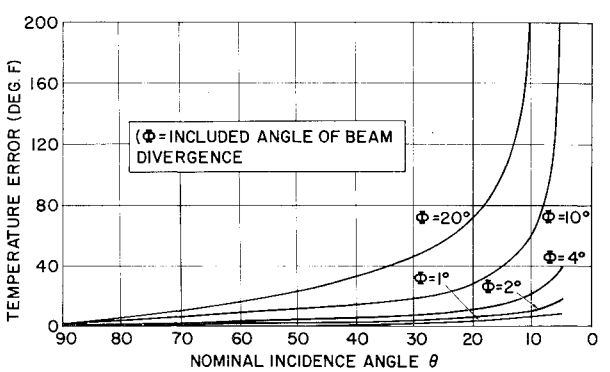

Fig. 1 Incidence angle errors as a function of solar simulator beam divergence.

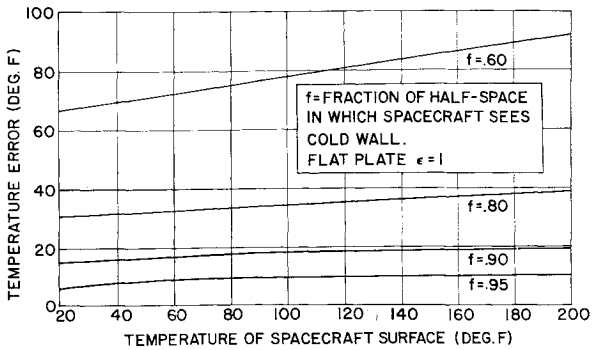

Fig. 2 Infrared reflection errors from solar simulator optics.

from the spacecraft will be returned to the cryogenic wall of the chamber and not the test object. In such a system the spacecraft will see by reflection only cryogenic wall in the collimators, thus achieving the effect of a continuous cryogenic wall about the test volume.

Some magnitudes of reflection errors from thermal energy emitted by a test object are shown in Fig. 2, where f is the fraction of half-space in which a point on the spacecraft sees the cold wall directly or by reflection off the collimating mirrors. The quantity $(1 - f)$ is a measure of half-space in which the spacecraft sees some part of itself by reflection.

Emission errors are the result of the thermal radiation emitted from the solar simulator optical elements. This error can be reduced by cooling the optics to low temperatures where the emitted energy is small, or by maintaining a low emittance coating on the surface of these elements. Either method is suitable for reducing the emitted energy to a level near that which would be expected from the cryogenic wall; however, cooling the optics may result in the distortion of these elements and may cause vapors in the chamber to condense on them, which would degrade their reflective characteristics during a test.

The reflective coating on collimating elements is usually aluminum, although the emissivity of aluminum (about 0.03 in the infrared) is not sufficiently low to reduce the thermal radiation from the collimators at ambient temperature to that of a liquid nitrogen cryogenic wall. However, the resulting thermal error for a spacecraft, at near ambient temperatures, will be very small even if the collimators occupy as much as one-third of a hemisphere of the space environment chamber.

Radar Video Data Handling

THOMAS J. BURKE*
Radio Corporation of America, Moorestown, N. J.

FOR years the exclusive function of the monopulse radar has been to acquire and track a single target, with emphasis on the radar spherical coordinate data, AGC, servo errors, and alignment errors for obtaining precise post flight trajectory measurements. Until recently, little attention has been given to monopulse radar data which gives information on all targets illuminated in the radar beam—the video information, which consists of the detected i.f. data from the radar receivers. The tracked target data is gated and used in the range and angle tracking loops to maintain automatic lock-on,

Presented as Preprint 63081-63 at the AIAA Space Flight Testing Conference, Cocoa Beach, Fla., March 18–20, 1963; revision received October 15, 1963.

* Leader, Data Handling Systems.

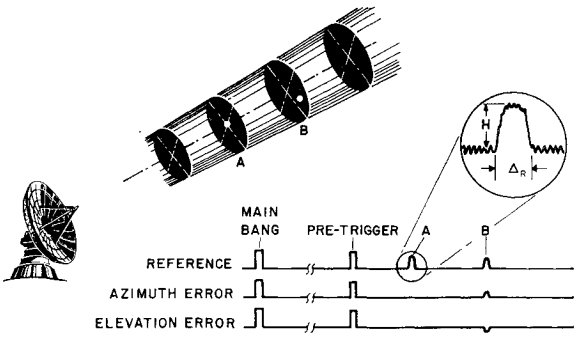

Fig. 1 Radar video.

and the ungated video provides information on untracked targets. The main bang or transmit pulse is emitted by the radar and the return echoes are received by the same antenna.

In Fig. 1, target A is the tracked target and target B is another target offset from the radar line of sight. The video from the azimuth and the elevation error receivers yield pulses which provide a measure of the offset of B, which can be accurately determined (through calibrations), and the amplitude (H) of the B target can be corrected to a value equivalent to that for a tracked target. Pretrigger pulses are precisely located relative to the A target, and the B target moves relative to them.

The transverse video record/playback system described below was made possible by developments in the TV industry. Subsequent advancements have been helical scan (continuous) recording, which eliminates the need for video multiplexing, and high-speed longitudinal recorders with up to 15 tracks for use with a multiple radar installation. The processing and reduction methods for such improved systems would be identical to those described here.

Video Recording

Video data are recorded by equipment (Fig. 2) which closely resembles standard TV studio recorders. The general TV requirements of frequency response (4 Mc) and signal/noise ratio (36 db) closely satisfy the requirements of radar video recording. However, the timing stability must be improved to give short- and long-term stabilities of approximately 10^{-5}. The radar return signals are processed in the microwave section, from which the azimuth and elevation signals are mixed with the local oscillator, and 30-Mc i.f. outputs are available to the receivers.

The reference signal represents the total energy received by the radar, and the azimuth and elevation error signals represent the difference between the target positions in their planes. The phase relations between the i.f. reference and error signals determine the directions of deviation, and the relative amplitudes between the i.f. reference and error signals determine the deviations. These three channels are fed to the wide dynamic range (WDR) receivers, which provide linear logarithmic amplification (without gating or gain control), which is maximum on weak signals and minimum on strong signals.

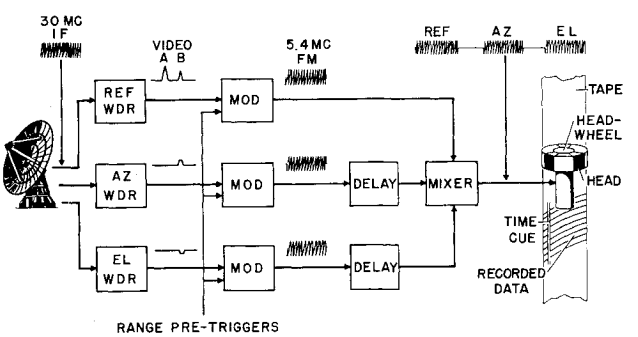

Fig. 2. Radar video recording.